

Synthesis and shape memory behavior of hyperbranched polyimides from thiol-ene click reaction

Y. F. Lu¹, Y. M. Wang¹, X. D. Chen², M. H. Miao³, D. H. Zhang^{1*}

¹Key Laboratory of Catalysis and Energy Materials Chemistry of Ministry of Education & Hubei Key Laboratory of Catalysis and Materials Science, South-Central University for Nationalities, 430074 Wuhan, China

²Key Laboratory for Polymeric Composite and Functional Materials of Ministry of Education, Key Laboratory of High Performance Polymer-based Composites of Guangdong Province, School of Chemistry, Sun Yat-Sen University, 510275Guangzhou, China.

³CSIRO Manufacturing, 75 Piggons Road, Waurn Ponds, 3216 Victoria, Australia

Received 7 June 2019; accepted in revised form 9 August 2019

Abstract. Shape memory polymers (SMPs) with novel functions have received increasing attention, but hyperbranched polyimide (HBPI)-based SMPs have rarely been reported. Herein, we have synthesized a series of thiol-ended hyperbranched polyimides (BTMP-*n*, *n* = 6, 9, 11) with various molecular weights using a thiol-ene click reaction, and BTMP-*n* was used as a crosslinking agent with 1-methacryl-allyl ethoxyethyl-diphenyl phosphate (AGDP) to prepare SMPs (BTMP-*n*-AGDP). The chemical structure and molecular weight of BTMP-*n* were characterized by Fourier transform infrared (FTIR) spectroscopy, proton nuclear magnetic resonance (¹H NMR) spectroscopy, and matrix-assisted laser desorption ionization time-of-flight (MALDI-TOF) mass spectroscopy. The shape fixity ratios and shape recovery ratios of BTMP-*n*-AGDP were over 99% and over 90%, respectively, indicating excellent shape memory properties. The excellent cycling stability of BTMP-*n*-AGDP was also demonstrated using the shape recovery sharpness over consecutive cycles. A rapid transition between the temporary shape and permanent shape of the BTMP-*n*-AGDP was discovered using the large shape recovery sharpness and a cramped strain recovery transition breadth. The results provide a new method for obtaining high-performance SMPs.

Keywords: smart polymers, shape memory, hyperbranched polyimides, click reaction

1. Introduction

As an important group of smart materials, shape memory polymers (SMPs) have received much attention in recent years [1]. The temporary shape of SMPs can recover to the permanent (or original) shape when the environmental conditions, such as pH, light, or temperature change [2–3]. Two prerequisites for the shape memory effect (SME) are a reversible switching transition and stable polymer network [4]. The original shape of SMPs is determined by the stable network, which can be formed by a crystalline phase, chemical cross-linking, or interpenetrating networks, etc. However, the temporary shape of SMPs is

determined by the reversible switching transition, which can be a glass transition, melting/crystallization transition, or liquid crystal isotropic/anisotropic transition [4–5]. There are many types of SMPs, but, according to the nature of the stimuli, all SMPs can be classified into three types only [6], namely, chemo-responsive SMPs (such as pH-responsive SMPs [7, 8]), thermo-responsive SMPs (including heating and cooling, either direct or indirect heating, such as thermal-responsive SMPs [9, 10] and electro-responsive SMPs [11, 12]) and photo-responsive SMPs. Dual SMPs [13], triple SMPs [14] and multiple SMPs [15, 16] can be obtained via programming.

*Corresponding author, e-mail: zhangdh27@163.com
© BME-PT

SMP materials can easily be produced in many specified shapes, such as thin films or foams with various porosities, and their shapes can change and then recover through changes in environmental conditions. In addition, the shape recovery temperature range of SMPs with highly recoverable strain can be easily controlled. Therefore, SMPs have found widespread use in fields including energy, electronic engineering, textiles, bionics engineering, civil engineering, and household products [4, 17]. However, during the past decade, research focused on SMPs such as polyurethanes (PU) [18] and polylactides [19] with relatively poor mechanical properties [20]. Their applications in soft robotics, smart textiles, actuators, and artificial muscles also have been studied [21], but their low mechanical strength limits their applications. Common approaches, including the introduction of functional end-groups and the design of polymers with high-density crosslinking structures [22, 23], have been used to increase the recovery stress and mechanical strength of SMPs. Microfibers, fabrics, mats, and carbon nanotubes can remarkably increase the mechanical strength of SMPs [4].

Polyimides (PIs) have been used in SMPs because of their outstanding thermal and chemical stabilities and excellent mechanical strength [24, 25]. Polyimide-based SMPs with high temperature [26–29] and ultrahigh strain [30] shape memory materials have been reported, and these polyimide-based SMPs also have been developed for applications in deployable structures with potential in-space flexible electronics used in harsh environments [31]. Nevertheless, the rigid molecular chains and strong inter-chain interactions mean that traditional aromatic PIs have trouble dissolving in common organic solvents [24, 32]. PIs are commonly synthesized by the reaction between dianhydride and diamine, or between dianhydride and diisocyanate, requiring two-step reactions at high temperatures [33]. For example, PI-POSS shape memory hybrid films were thermally imidized at 60, 80, 100, 200 and 300 °C for 1 h [26], and other PI shape memory films were successively imidized at 80 °C for 4 h, 120 °C for 1 h, 140 °C for 1 h, 220 °C for 1 h, 280 °C for 1 h, and 320 °C for 1 h [34]. A rapid and highly efficient synthesis approach at low temperatures for PI-based SMPs remains a challenge that prevents their widespread application.

As a rapid and environment-friendly synthesis method, the click reaction shows high yield, high

efficiency, and stereospecificity, in addition to being a simple process to perform in easily removable solvents [35]. The thiol-ene reaction is one of the click chemistry reactions [36]. Hyperbranched polymers (HBPs) are tree-like macromolecules with abundant functional groups and densely branched globular shape that possesses low viscosity and high chemical reactivity, indicating their suitability for many applications in fields such as coatings, patterning, and biomaterials [37]. Among HBPs, hyperbranched polyimides (HBPIs) may be the ideal shape memory materials because of their simultaneous high mechanical properties and solubility. Furthermore, HBPI-based SMPs have rarely been reported, and the reported shape switching temperature is relatively high (>300 °C) [23]. Therefore, a HBPI-based SMP that has good shape memory behavior, good mechanical properties, and that can be synthesized using a rapid and highly efficient approach is needed. Herein, we synthesized a series of thiol-ended hyperbranched polyimides (BTMP-*n*, *n* = 6, 9, 11) with various molecular weights using a thiol-ene click reaction between *N*, *N*-(4, 4-methylene phenyl) bis-maleimide (BMI, A₂ monomer) and trimethylolpropane tris(3-mercaptopropionate) (TMMP, B₃ monomer). SMPs (BTMP-*n*-AGDP) were obtained utilizing UV curing-crosslinking technology involving BTMP-*n* and 1-methacryl-allyl ethoxyethyl-diphenyl phosphate (AGDP), a diolefin monomer. The tensile strength, thermal properties, and shape memory behavior of the cured BTMP-*n*-AGDP were studied in detail.

2. Experimental

2.1. Materials

4,4-bis(Maleimidophenyl)methane (BMI) was purchased from Honghu City Shuangma New Materials Tech Co., Ltd, Honghu, China. Trimethylolpropane tris (3-mercaptopropionate) (TMMP) was prepared according to our previous report [38]. 1-Methacryl-allyl ethoxyethyl-diphenyl phosphate (AGDP, diolefin monomer) was synthesized according to the literature [39]. 2,2-Dimethoxy-2-phenylacetophenone (DMPA, photo-initiator 651) was purchased from Shanghai Meryer Chemical Technology Co., Ltd, Shanghai, China. Triethanolamine (TEA), chloroform, and other organic solvents were purchased from Sinopharm Chemical Reagent Co., Ltd, Shanghai, China. All solvents and reagents were of analytical grade and were used as received.

2.2. Preparation of BTMP-*n* and BTMP-*n*-AGDP

2.2.1. Preparation of thiol-ended hyperbranched polymers (BTMP-*n*, *n* = 6, 9, 11)

According to Figure 1, thiol-ended hyperbranched polymers (BTMP-*n*) with various molecular weights were prepared via a thiol-ene click reaction between BMI and TMMP. The detailed preparation process for BTMP-6, with six molar thiol groups, is given as follows. Under a nitrogen atmosphere, BMI (7.17 g, 0.02 mol), TMMP (10.63 g, 0.027 mol), chloroform (120 ml), and two drops of TEA as catalyst were added to a 250 ml three-necked flask. The solution was heated for 24 h at 60 °C under nitrogen flow and stirring with a magnetic stirrer. The solvent was removed using a rotary evaporator, and a yellow liquid (denoted BTMP-6) (16.38 g, 92%) was obtained. The other two yellow liquid products denoted as BTMP-9 and BTMP-11, which contain 9 and 11 molar thiol groups, respectively, were obtained by a similar process, but the ratio of BMI to TMMP was altered.

2.2.2. Preparation of SMPs (BTMP-*n*-AGDP)

The preparation process for BTMP-*n*-AGDP is shown in Figure 2. First, a mixture was formulated with BTMP-6 (13.35 g, 0.005 mol), AGDP (11.59 g, 0.03 mol) with a molar ratio of the thiol group to double bond of approximately 1:1, and a catalytic amount of DMPA (0.05 g) dissolved in chloroform. The homogeneous mixture was poured into a mold (the thicknesses of the samples were 0.2 and 0.1 cm, respectively) and placed into a UV reactor (UWave-2000, 365 nm, 300 W, Shanghai Sineo Microwave Chemistry Technology Co., Ltd., Shanghai, China) at a controlled temperature of 25 °C for 45 min. The cured samples (BTMP-6-AGDP) were removed from the mold and dried at 80 and 100 °C, respectively, for 2 h in a vacuum oven. Two other cured samples were obtained using a similar process and denoted BTMP-9-AGDP and BTMP-11-AGDP, respectively.

2.3. Characterization

ATR-FTIR data were obtained using a spectrometer (Bruker Vertex 70, Germany). ¹H NMR data were

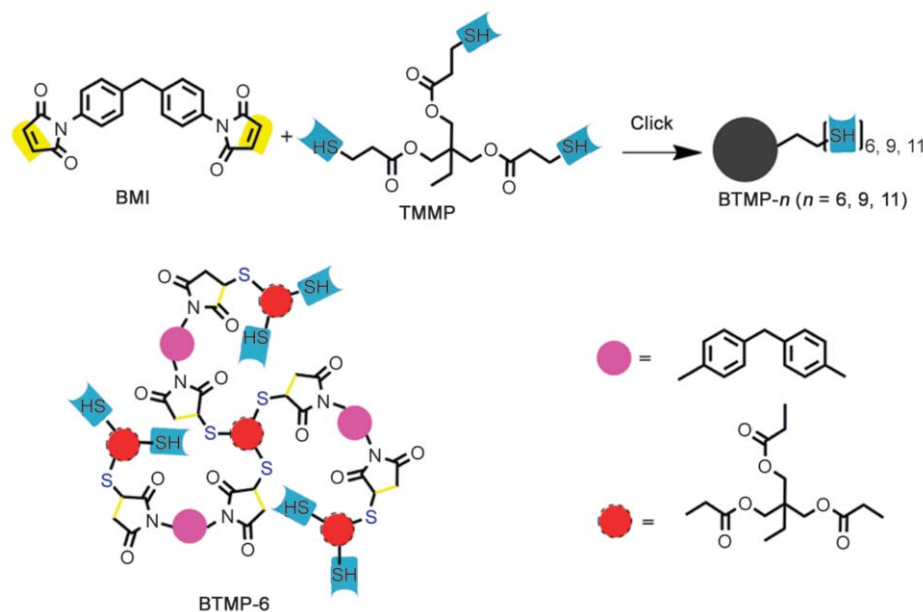


Figure 1. Synthesis scheme for BTMP-*n* (*n* = 6, 9, 11) and the chemical structure of BTMP-6.

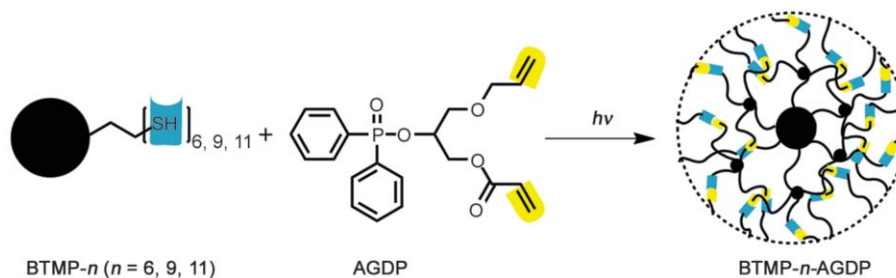


Figure 2. Synthesis scheme for BTMP-*n*-AGDP.

recorded on a spectrometer (Bruker Avance III 400 MHz, Germany) with DMSO-d₆ as a solvent and tetramethylsilane as the internal standard. MALDI-TOF mass spectra studies were conducted with a Bruker MALDI-TOF system (Germany) using chloroform as a solvent; the concentration of BTMP-*n* in the solution was 10 mg/ml, and α -cyano-4-hydroxycinnamic acid (CHCA) was employed as the matrix. Thermogravimetric analysis (TGA) was conducted using a thermogravimetric analyzer (NETZSCH TG209, Germany) under a 20 ml/min nitrogen flow and a 10 K/min heating rate. The tensile strength of the BTMP-*n*-AGDP samples (4 cm×0.5 cm×0.2 cm) was characterized using a tensile testing machine (Instron 5966, Instron, Norwood, MA, USA) at a loading rate of 5 mm/min according to ASTM D638-14. Dynamic mechanical thermal analysis (DMA) was conducted on the BTMP-*n*-AGDP samples (4 cm×1 cm×0.1 cm) using a DMA Q800 instrument (TA Instruments, USA) in multi-frequency-strain mode. The frequency was 1 z, and the heating rate was 10 K/min from 273 to 423 K. The shape-memory cycle behavior of the BTMP-*n*-AGDP samples (4 cm×1 cm×0.1 cm) was investigated using force-controlled mode.

3. Results and discussion

3.1. Characterization of BTMP-*n*

The ATR-FTIR spectra of BMI, TMMP, and BTMP-*n* are presented in Figure 3a. In the TMMP spectrum, the stretching vibration peak of the –CH₂– group is at 2966 cm⁻¹; the characteristic peak of the SH group is at 2569 cm⁻¹; the strong stretching vibration peak of the C=O bond is at 1734 cm⁻¹; the bending vibration peaks of C–H are between 1150 and 1381 cm⁻¹; and the stretching vibration peaks of C–O and C–O–C in the ester group are at 1247, 1120 and 1066 cm⁻¹. In the spectrum of BMI, the peaks at 3102 and 2913 cm⁻¹ correspond to the stretching vibration of C–H, the strong peak at 1713 cm⁻¹ corresponds to the stretching vibration of the C=O group, and the peak at 1612 cm⁻¹ corresponds to the stretching vibration of C=C. The peaks at 1513 and 1589 cm⁻¹ correspond to the bending vibration of C=C in the benzene ring. The peak at 1391 cm⁻¹ corresponds to the stretching vibration of O=C–N in the imine ring. The peaks at 831 and 689 cm⁻¹ correspond to the imine =CH out-of-plane bending and imine framework vibration. After the reaction, the signals of the strong peaks of C=O stretching vibration in TMMP

(1734 cm⁻¹) and BMI (1713 cm⁻¹) shifted to 1723 cm⁻¹ in BTMP-*n*. Moreover, the C=C (1612 cm⁻¹) characteristic peak and the peaks at 831 and 689 cm⁻¹ resulting from the imine =CH out-of-plane bending and imine framework vibration were almost non-existent in the BTMP-*n*; also, the SH group (2569 cm⁻¹) in BTMP-*n* was present. Other peaks of functional groups in the BMI and TMMP were also found in the FTIR spectrum of BTMP-*n*. All of the above evidence suggests that the thiol-maleimide reaction occurred on BTMP-*n* [40].

The ¹H NMR spectra of BTMP-*n* are illustrated in Figure 3b. In the BTMP-6 spectrum, after the click reaction, the peaks of C=C bond protons in the imine ring disappeared and new peaks appeared at 3.35–3.25 ppm (H_k, H_i,) and 3.05 ppm (H_j) of the –S–CH–CH₂– protons [41]. The peaks of protons in the benzene ring appeared at 7.35, 7.23 (H_{m1}, H_{m2}); the signals of the protons of H_c, H_i, H_e, H_h, H_{d,g}, and H_b were found at 4.02, 3.95, 2.95, 2.67, 2.65, and 1.32 ppm, respectively; and the peak at 0.84 ppm can be attributed to the protons of CH₃ (H_a). The ¹H NMR spectra of BTMP-9 and BTMP-11 are similar to the spectra of BTMP-6.

Figure 3c and 3d shows MALDI-TOF mass spectra of BTMP-*n*. Each spectrum consists of a series of signals of fragmentation related to the TMMP and BMI units. As shown in Figure 3d for BTMP-9, the spectrum contains ten sets of main signals:

- a:** [(C₁₅H₂₆O₆S₃)+(C₂₁H₁₄N₂O₄)₃](Na⁺) (1498 *m/z*),
- b:** [(C₁₅H₂₆O₆S₃)₂+(C₂₁H₁₄N₂O₄)₃](Na⁺) (1900 *m/z*),
- c:** [(C₁₅H₂₆O₆S₃)₂+(C₂₁H₁₄N₂O₄)₄](Na⁺) (2256 *m/z*),
- d:** [(C₁₅H₂₆O₆S₃)₃+(C₂₁H₁₄N₂O₄)₄](Na⁺) (2658 *m/z*),
- e:** [(C₁₅H₂₆O₆S₃)₃+(C₂₁H₁₄N₂O₄)₅](Na⁺) (3015 *m/z*),
- f:** [(C₁₅H₂₆O₆S₃)₄+(C₂₁H₁₄N₂O₄)₅](Na⁺) (3416 *m/z*),
- g:** [(C₁₅H₂₆O₆S₃)₄+(C₂₁H₁₄N₂O₄)₆](Na⁺) (3773 *m/z*),
- i:** [(C₁₅H₂₆O₆S₃)₅+(C₂₁H₁₄N₂O₄)₆](Na⁺) (4169 *m/z*),
- j:** [(C₁₅H₂₆O₆S₃)₆+(C₂₁H₁₄N₂O₄)₆](Na⁺) (4562 *m/z*),
- and **k:** [(C₁₅H₂₆O₆S₃)₇+(C₂₁H₁₄N₂O₄)₆] (4941 *m/z*).

These signals can be assigned to a structure with TMMP as the core and poly(BMI-TMMP) as dendritic chain extender units. Other small signals are related to the main signal structure with some groups lost (such as –CH₃) [42]. The *m/z* of the largest fragmentation signal is 4941, which shows that the molecular weight of BTMP-9 is 4941 g/mol, being very close to the theoretical molecular weight (4940 g/mol) calculated from the molar ratio of BMI to TMMP. The MALDI-TOF mass spectra of BTMP-6 and BTMP-11 are similar to the spectra of BTMP-9 in

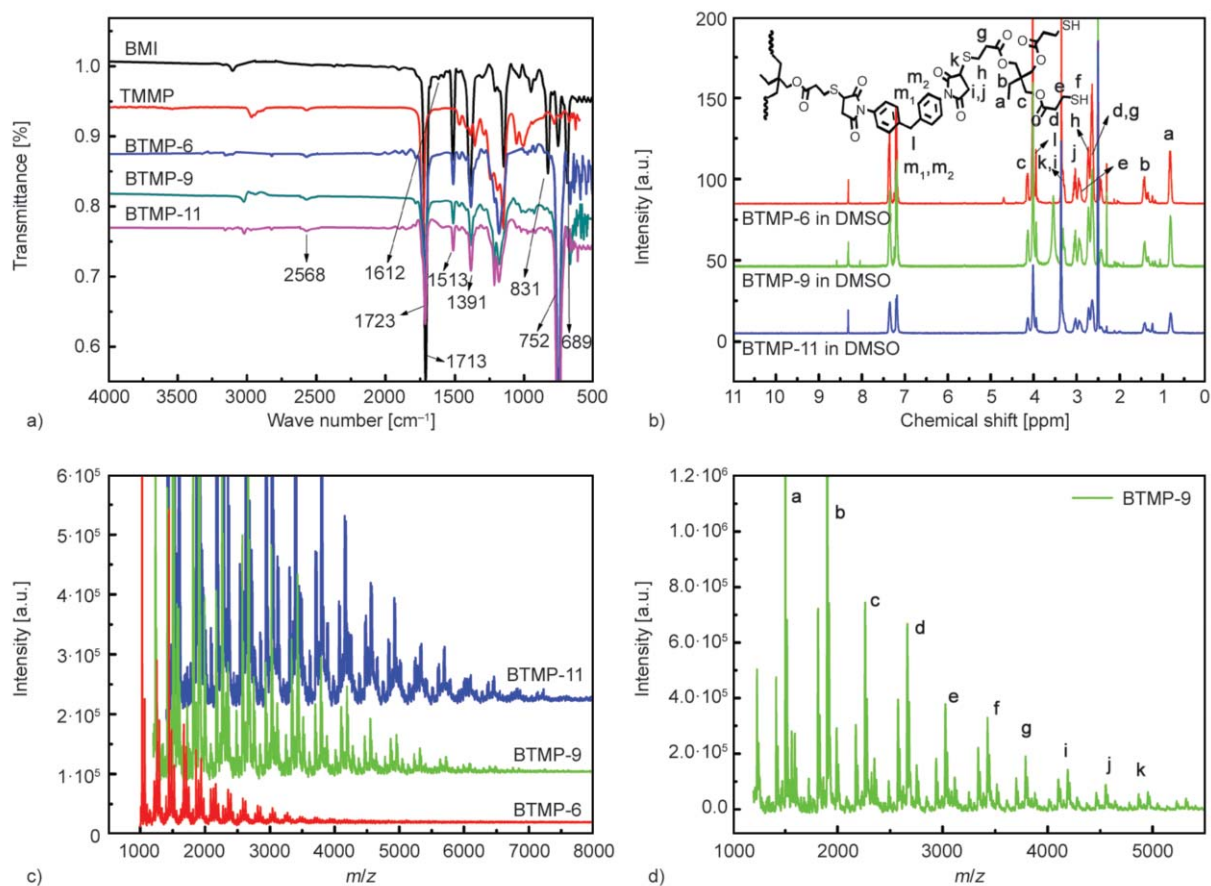


Figure 3. ATR-FTIR (a), ^1H NMR (b), and MALDI-TOF mass (c, d) spectra of BTMP- n .

Figure 3c. The molecular weights of BTMP-6 and BTMP-11 are 2660 and 6500 g/mol, respectively, which are very close to their theoretical molecular weights (2669 and 6454 g/mol, respectively) calculated from the molar ratio of BMI to TMMP, demonstrating that the molecular weights of BTMP- n increase as their thiol groups increase. In summary, the results of ATR-FTIR, ^1H NMR, and MALDI-TOF mass spectra suggest that the BTMP- n were synthesized with a thiol-maleimide click reaction.

3.2. Shape memory behavior of BTMP- n -AGDP

The loss tangent ($\tan \delta$) and storage modulus (E) of BTMP- n -AGDP were assessed using a DMA Q800, and their curves, with respect to the temperature, are shown in Figure 4a, 4b. The glass transition temperature (T_g) data for BTMP- n -AGDP are listed in Table 1. The reason why Figure 4b shows two T_g may be that a small amount of AGDP is self-polymerizing. At the rubber stage and with the rubber elasticity model [43–45], the valid crosslinking density (ν_e) of BTMP- n -AGDP is a function of the storage modulus (E) and temperature (T) as shown in Equation (1):

Table 1. T_g data for BTMP- n -AGDP.

Sample	T_{g1} [°C]	T_{g2} [°C]
BTMP-6-AGDP	46.3±0.4	82.2±0.2
BTMP-9-AGDP	58.8±0.2	90.4±1.0
BTMP-11-AGDP	39.6±0.5	80.5±0.1

T_g : glass transition temperature

$$\nu_e = \frac{E}{3\psi RT} \quad (1)$$

where ψ is the front factor (usually equal to 1) and R is the gas constant. Measuring the crosslinking density uses the rubbery modulus, which is the E at $T_{g2} + 40^\circ\text{C}$. The result for ν_e is shown in Figure 4c. Figure 4 shows that the T_g and storage modulus (E) both first increased then decreased, but the crosslinking density increased continuously as the BTMP- n molecular weight increased. This result can be explained by the crosslinking density [46] and a rigid chain of BTMP- n -AGDP. The thiol groups of BTMP- n were enhanced when the molecular weight of BTMP- n increased, which led to an increase in the T_g and storage modulus (E) of BTMP- n -AGDP.

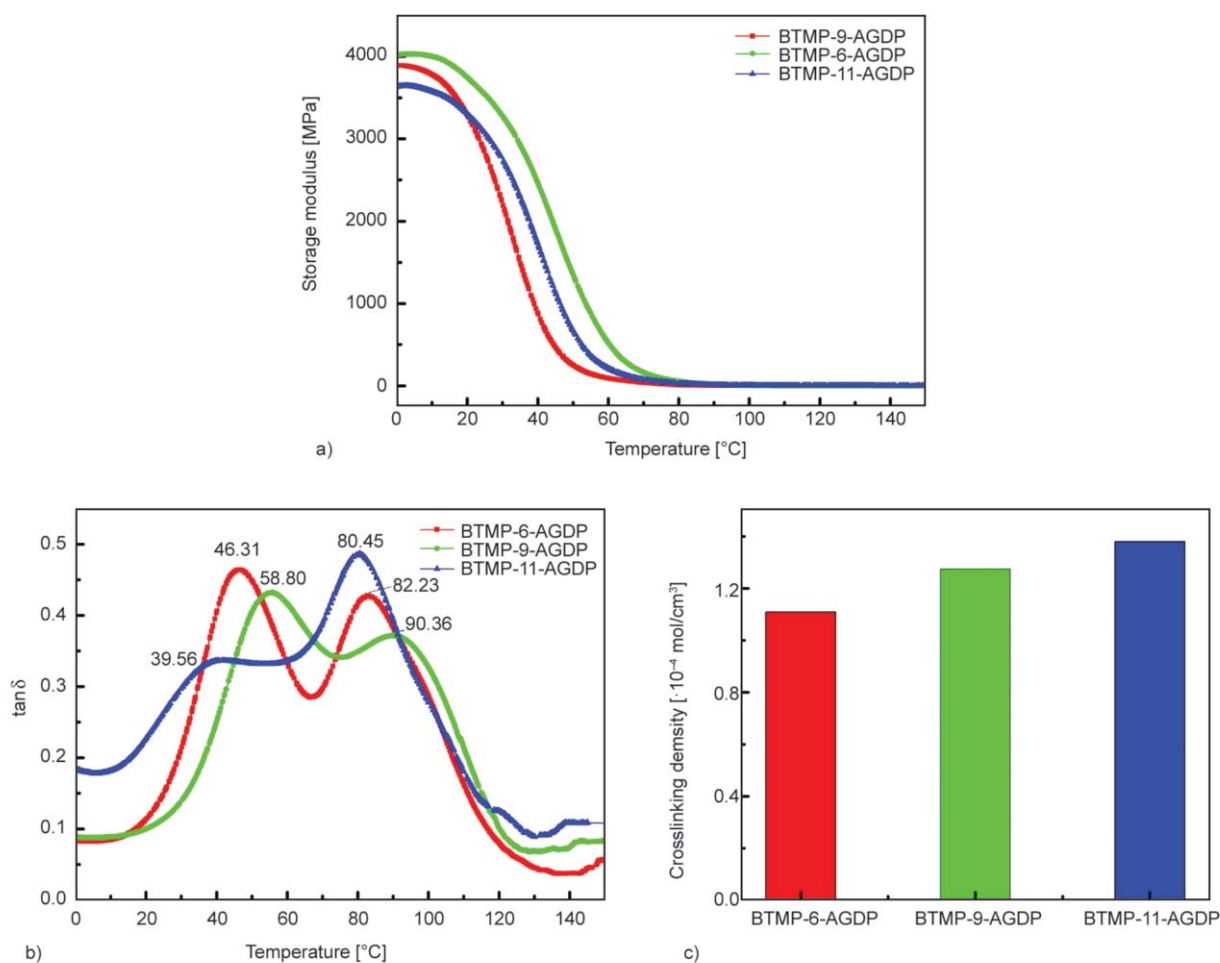


Figure 4. DMA curves of BTMP-*n*-AGDP, a) storage modulus; b) $\tan \delta$; c) crosslinking density.

However, the rigid chain of BTMP-*n*-AGDP decreased as the molecular weight of BTMP-*n* increased, which caused the T_g and storage modulus (E) to decrease. This explains why the T_g and storage modulus (E) reached a maximum as the molecular weight of BTMP-*n* increased.

The temporary shape of SMPs can recover to their permanent shape when the environmental conditions change (temperature, pH, etc.). The original (or permanent) shape of the sample can deform at the deformation temperature (T_d) and then become fixed at a temporary shape at the fixity temperature T_f ($T_f < T_d$); finally, at the recovery temperature T_r ($T_r \geq T_d$), the temporary shape can be restored to the original shape. Herein, the deformation temperature (T_d) of shape-memory BTMP-*n*-AGDP is close to the glass transition temperature (T_{g2}) [47], which can be taken from the maxima in Figure 4b. The T_d values of BTMP-6-AGDP, BTMP-9-AGDP, and BTMP-11-AGDP were 83, 91, and 81 °C, respectively. Assessing the shape-memory properties of BTMP-*n*-AGDP using the tensile and fold-deploy test is shown in

Figure 5. As exhibited in Figure 5a, the original shape (permanent shape, ϵ_0) of BTMP-6-AGDP was first set at the deformation temperature $T_d = 83$ °C, and then BTMP-6-AGDP was cooled to $T_f = 30$ °C with a temporary shape (ϵ_1). Upon reheating the sample to $T_r = 83$ °C, the temporary shape changed back to the original shape ($\epsilon_{0, re}$). Figure 5b and 5c show that BTMP-9-AGDP and BTMP-11-AGDP followed a similar process at $T_d = 91$ and 81 °C, respectively. The gradual recovery process of BTMP-6-AGDP was captured in photographs and shown in Figure 5d. First, the temporary shape of the BTMP-6-AGDP sample was reheated to 83 °C, and then the BTMP-6-AGDP sample recovered to approximately 50% of its permanent shape after two seconds; finally, the BTMP-6-AGDP sample completely recovered to its original shape. The shape recovery time was approximately 4.5 s, which is excellent in comparison with recently published results [24, 31].

The behavior of shape-memory-cycle was measured by a DMA Q800. As shown in Figure 6, first, the BTMP-6-AGDP sample was heated to 83 °C (T_d)

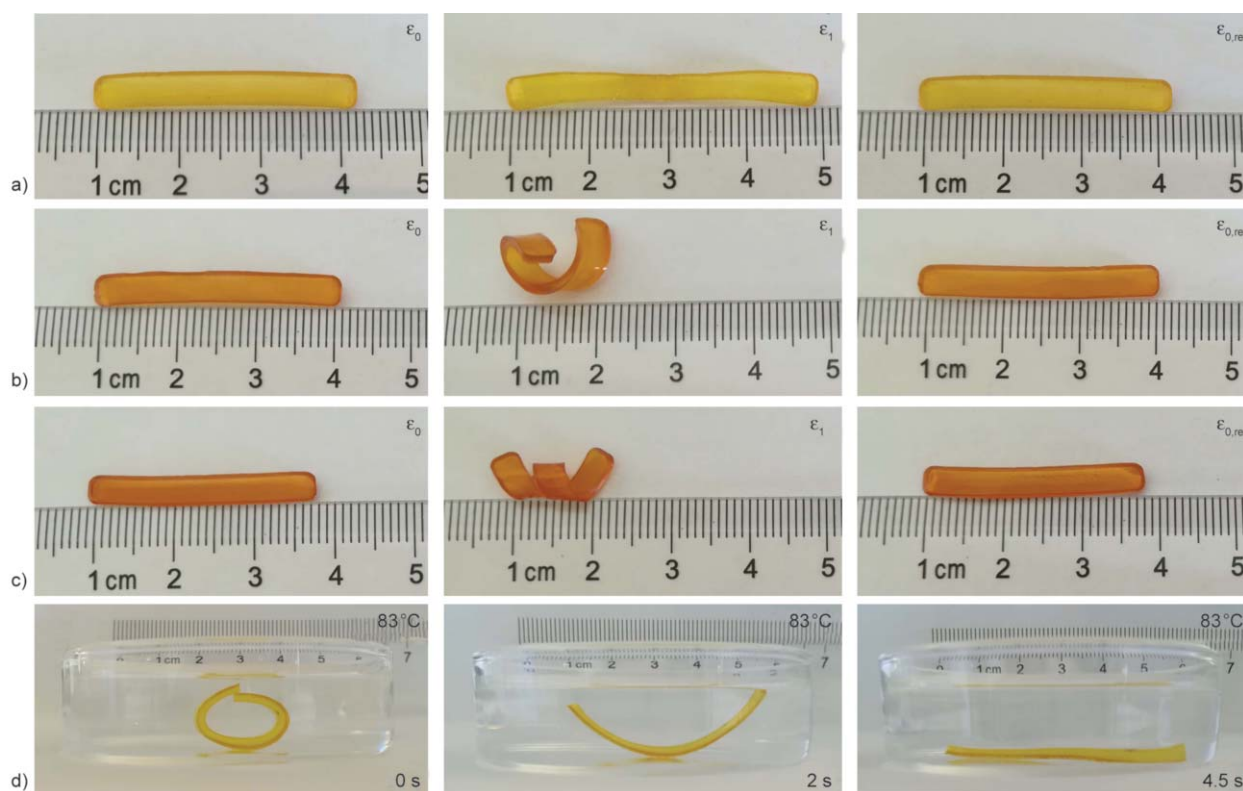


Figure 5. Images of the deploying and recovery process for BTMP-*n*-AGDP, a) BTMP-6-AGDP, b) BTMP-9-AGDP, c) BTMP-11-AGDP, d) gradual recovery process of BTMP-6-AGDP.

and then equilibrated at that temperature for 10 min before being tested for shape memory. During this process, the sample undergoes thermal expansion, and the strain (ϵ_0) on the sample after the expansion was measured. Second, at a stress ramping rate of 0.3 N/min and at 83 °C, the sample was deformed until the required strain (ϵ_1) was obtained. Then, keeping the force constant and at a cooling rate of 5 °C/min, the temperature was lowered to the fixity temperature (T_f). After being kept for 10 min at T_f , the sample strain was labeled ϵ_1 and a stress ramping rate of 0.3 N/min was used to unload the force to 1 mN. After the external force unloading, the temporary shape of BTMP-6-AGDP was fixed for 5 min, and the sample strain was labeled ϵ_2 . Finally, using a heating rate of 5 °C/min, the sample was reheated to the recovery temperature (T_r , $T_r = T_{g2}$) and kept at that temperature for 10 min; the final strain of the BTMP-6-AGDP sample was labeled ϵ_3 . This cycle was repeated four times for the BTMP-6-AGDP sample. The procedures for both BTMP-9-AGDP and BTMP-11-AGDP were similar to that for BTMP-6-AGDP. To quantify the shape memory behavior, the most significant parameters are the shape fixity ratio (R_f), shape recovery ratio (R_r), and shape recovery sharpness (v_r). The ability to maintain a temporary

shape under T_{g2} is quantified by R_f . The ability to recover to the permanent shape is quantified by R_r . Shape recovery sharpness (v_r) characterizes the speed whereby the sample recovers to its permanent shape from a temporary shape. These parameters are defined as shown in Equations (2)–(4): [47, 48].

$$R_f = \frac{\epsilon_2(N) - \epsilon_0(N)}{\epsilon_1(N) - \epsilon_0(N)} = \frac{\epsilon_2(N) - \epsilon_3(N-1)}{\epsilon_1(N) - \epsilon_3(N-1)} \quad (2)$$

$$R_r = \frac{\epsilon_2(N) - \epsilon_3(N-1)}{\epsilon_2(N) - \epsilon_3(N-1)} \quad (3)$$

$$v_r = \frac{0.8}{T_{90} - T_{10}} \cdot 100\% \quad (4)$$

where N is the thermal-mechanical cycle number, ranging from 1 to 4, and T_{10} and T_{90} are the temperatures corresponding to R_r of 10% and 90%, respectively, in every cycle. The values of R_f , R_r , and v_r for BTMP-*n*-AGDP are shown in Table 2. As shown in Figure 6 and Table 2, when BTMP-*n*-AGDP was exposed to four subsequent shape memory cycles, the R_f value of BTMP-*n*-AGDP was >99% and R_r value was >90%, except for the first cycle of the thermal expansion. The R_f and R_r of each sample did not change significantly after four cycles, indicating excellent cycling stability. In the fourth cycle, the shape

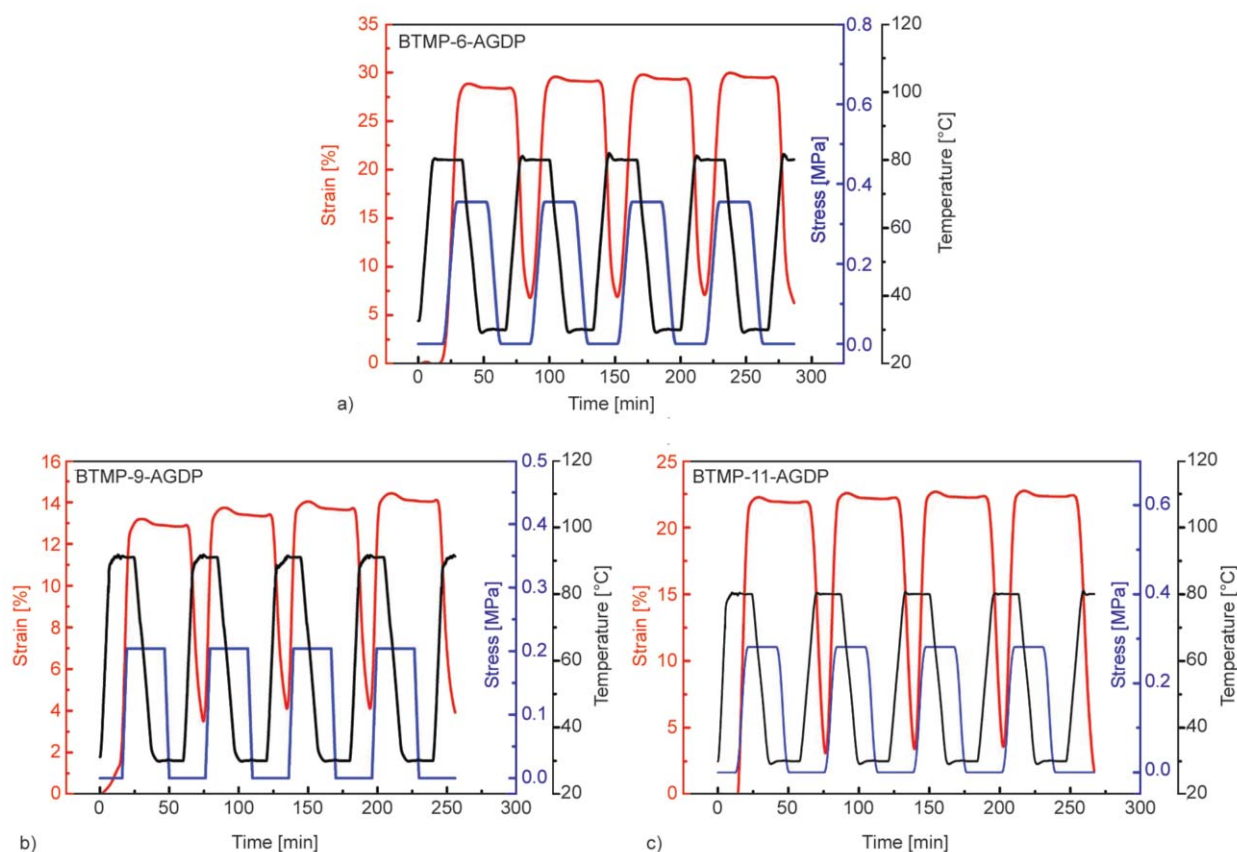


Figure 6. The shape-memory-cycle behavior of a) BTMP-6-AGDP, b) BTMP-9-AGDP, and c) BTMP-11-AGDP.

recovery ratio was $>100\%$ because the value reflects the combined effect of the shape recovery and the thermal expansion. The cycling stability of BTMP- n -AGDP can also be demonstrated using the shape recovery sharpness (v_r) over consecutive cycles. After the initial training, the v_r of BTMP-6-AGDP remained above $6.8\%/^{\circ}\text{C}$ (Table 2) in the first cycle and subsequent cycles with little change. BTMP-9-AGDP shows lower but also consistent v_r values (4.5 – $5.4\%/^{\circ}\text{C}$), while BTMP-11-AGDP shows higher v_r values (10.1 – $12.3\%/^{\circ}\text{C}$). A rapid transition between the temporary shape and permanent shape of the

BTMP- n -AGDP was demonstrated by the large shape recovery sharpness and a cramped strain recovery transition breadth [49]. This is primarily a result of the sharp and large decrease in storage modulus (E) at T_g , which is an important characteristic for ideal SMP materials [24, 31].

The SME of BTMP- n -AGDP can be explained using the phase evolution modeling method [47, 50]. The polymer model always shows an active phase and frozen phase when the temperature is in the transition region (T_g s). As shown in Figure 7, first, the sample is in a rubbery state completely (red area)

Table 2. Shape memory performance of BTMP- n -AGDP.

Sample	Cycle	Cycle			
		1	2	3	4
BTMP-6-AGDP	R_f [%]	99.7 ± 0.5	99.7 ± 1.0	99.7 ± 0.3	99.8 ± 0.6
	R_r [%]	76.0 ± 1.2	99.6 ± 0.6	99.6 ± 0.8	103.8 ± 0.6
	v_r [%/ $^{\circ}\text{C}$]	6.8 ± 0.2	6.4 ± 0.3	6.9 ± 0.3	6.7 ± 0.5
BTMP-9-AGDP	R_f [%]	99.6 ± 0.6	99.6 ± 0.6	99.7 ± 0.8	99.7 ± 1.0
	R_r [%]	72.9 ± 1.2	93.9 ± 0.9	99.5 ± 0.8	102.1 ± 0.7
	v_r [%/ $^{\circ}\text{C}$]	4.5 ± 0.7	5.4 ± 0.6	4.9 ± 0.3	5.0 ± 0.8
BTMP-11-AGDP	R_f [%]	99.8 ± 1.2	99.7 ± 1.3	99.8 ± 1.0	99.8 ± 1.1
	R_r [%]	91.8 ± 1.0	98.3 ± 0.9	99.2 ± 1.3	109.6 ± 1.3
	v_r [%/ $^{\circ}\text{C}$]	10.1 ± 0.3	10.5 ± 0.5	11.1 ± 0.6	12.3 ± 1.0

R_f : shape fixity ratio; R_r : shape recovery ratio; v_r : shape recovery sharpness.

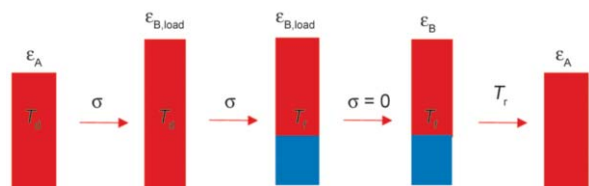


Figure 7. SME mechanism of BTMP-*n*-AGDP.

when the sample is heated to T_d ($T_d = T_g$). When tensile stress, σ , is loaded to the sample, a strain $\epsilon_{B,load}$ on the sample is obtained. Then, the polymer chains of the fractional compositions are frozen (aqua area), which is greater than the T_f of fractional T_g 's when the sample is cooled to T_f ($T_f < T_g$), with the result that this part of the elastic energy is frozen. When the stress on the sample is unloaded ($\sigma = 0$), a spontaneous spring-back is produced because the unfrozen elastic energy of a portion of the unfrozen polymer chains is released, leading the sample to shrink. Thus, the sample obtains a temporary shape (ϵ_B). Finally, the fully frozen sample is heated to T_r again and the sample recovers its permanent (original) shape (ϵ_A) because the stored elastic energy is released.

Therefore, the unique crosslinked networks and the entropic elasticity of molecular segments ensure the excellent shape memory properties of BTMP-*n*-AGD. The molecular segments of AGDP act as a reversible phase that can be frozen and reactivated during the glass transition, while BTMP-*n* linkages behave as a fixation phase because of its hyperbranched structure, thus ensuring the high shape fixity ratio (R_f) and shape recovery ratio (R_r) of BTMP-*n*-AGDP [51].

3.3. Performance of BTMP-*n*-AGDP

The thermal stability of BTMP-*n*-AGDP was assessed using TGA. Figure 8a shows the decomposition behavior of BTMP-*n*-AGDP, obtained using TGA. The decomposition temperatures corresponding to 5% weight loss (T_5) and 10% weight loss (T_{10}) and the temperatures of the maximum degradation rate (T_{max}) and char yield at 700 °C are listed in Table 3. T_5 and T_{10} of BTMP-*n*-AGDP first increased and then decreased with increasing BTMP-*n* molecular weight, but their T_{max} values showed little difference. The change in the T_5 and T_{10} of BTMP-

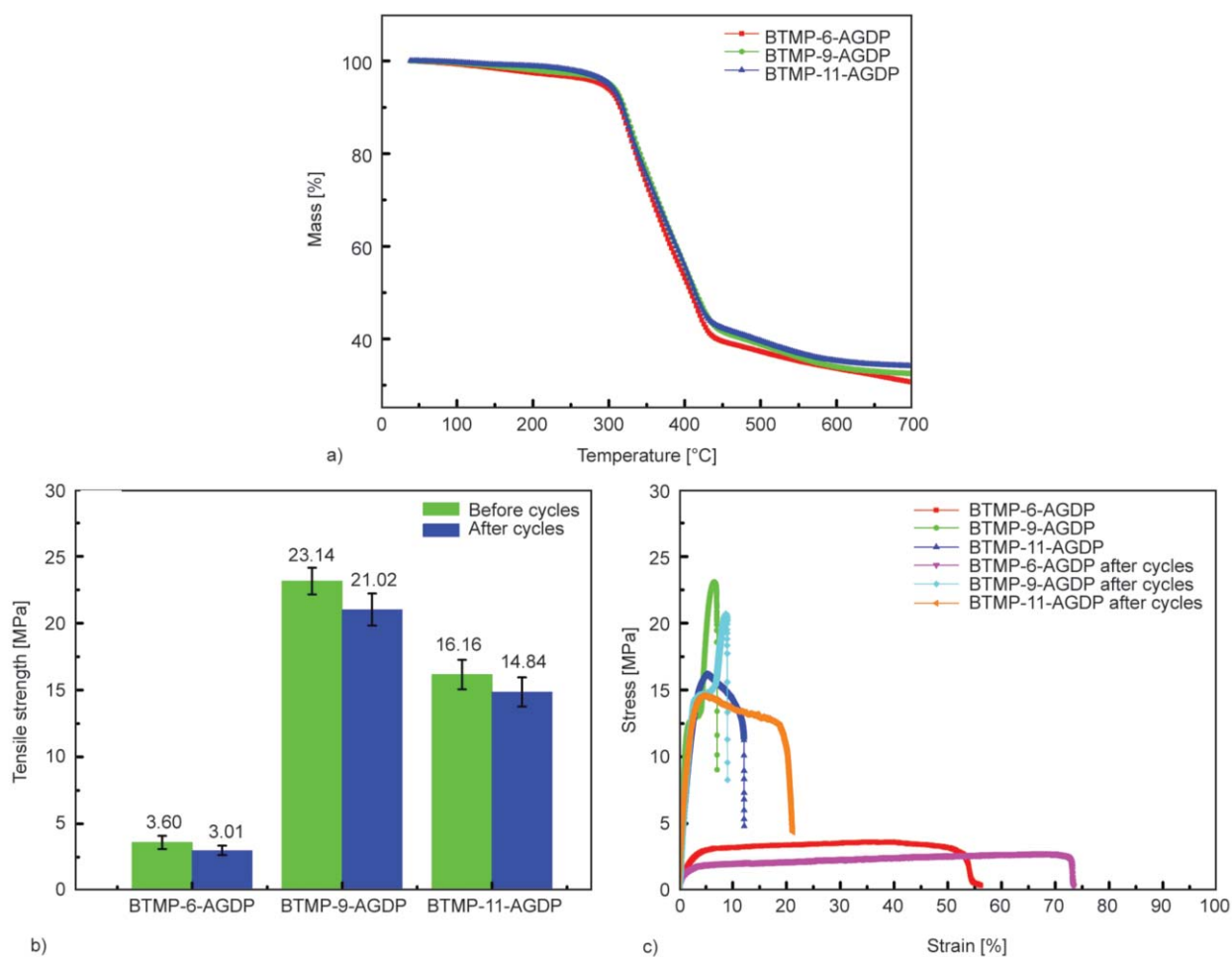


Figure 8. The performance of BTMP-*n*-AGDP, a) TGA, b) tensile, c) strain-stress curves.

Table 3. Thermal and tensile data for BTMP-*n*-AGDP.

Sample	T_5 [°C]	T_{10} [°C]	T_{max} [°C]	Char yield at 700 °C [wt%]	B-tensile strength ^a [MPa]	A-tensile strength ^b [MPa]	Retention rate [%]
BTMP-6-AGDP	290.5	315.3	328.3	30.66	3.60±0.50	3.01±0.35	83.61
BTMP-9-AGDP	301.5	320.4	327.2	32.51	23.14±1.00	21.02±1.20	90.84
BTMP-11-AGDP	300.1	318.1	326.5	34.14	16.16±1.10	14.86±1.09	91.96

T_5 : decomposition temperature of 5% weight loss in TGA;

T_{10} : decomposition temperature of 10% weight loss in TGA;

T_{max} : temperature of maximum degradation rate (T_{max});

^atensile strength before shape memory cycle analysis;

^btensile strength after shape memory cycle analysis.

n-AGDP can be attributed to the combined effect of cavities and nitrogen content of the BTMP-*n*. The cavities of the hyperbranched BTMP-*n* increased with increasing molecular weight, so the T_5 and T_{10} of BTMP-*n*-AGDP decreased. Furthermore, as the BTMP-*n* molecular weight increased, the nitrogen content of the BTMP-*n* increased, which may have caused an increase in T_5 and T_{10} .

The tensile performances of the BTMP-*n*-AGDP before and after shape memory cycle analysis are shown in Figure 8b, 8c, and the detailed data are summarized in Table 3. Before the shape memory cycle analysis, the tensile strengths of BTMP-6, BTMP-9, and BTMP-11 were 3.60, 23.14, and 16.16 MPa, respectively. The tensile strength increased first and then decreased as the BTMP-*n* molecular weight increased, but the elongation at break followed an opposite trend. This is influenced by the crosslinking density of BTMP-*n*-AGDP and the intramolecular cavities of BTMP-*n*. Crosslinking density enhances the tensile strength, while the effect of the intramolecular cavities is the opposite [52]. Both the content of intramolecular cavities and the crosslinking density of BTMP-*n*-AGDP increased as the BTMP-*n* molecular weight increased, resulting in a maximum as the molecular weight of BTMP-*n* increased. After the shape memory cycle analysis, the tensile strengths of BTMP-6, BTMP-9, and BTMP-11 were 3.01, 21.02, and 14.86 MPa, respectively, with respective retention rates of 83.61, 90.84, and 91.96%, showing a slight decrease in tensile strength. The elongation at break of BTMP-*n* also showed a slight increase after shape memory cycle analysis. The results for tensile strength and elongation at break probably occurred because the cross-linked network structure was slightly destroyed after shape memory cycle analysis. However, the retention rates of BTMP-*n*-AGDP were all over 8 %, which verifies the stability

of the cross-linked network structure of BTMP-*n*-AGDP as a result of its hyperbranched structure.

4. Conclusions

In summary, a series of thiol-ended hyperbranched polyimides (BTMP-*n*) with various molecular weights were synthesized by a thiol-ene click reaction; they were further fabricated into BTMP-*n*-AGDP utilizing UV curing-crosslinking technology. The chemical structure of BTMP-*n* was characterized by ATR-FTIR and ¹H NMR. The shape memory properties, tensile performance, and thermal properties of BTMP-*n*-AGDP were studied. The BTMP-*n*-AGDP membranes demonstrated excellent shape memory behavior, with a shape recovery ratio above 90% and shape fixity ratio above 99%. BTMP-*n*-AGDP also showed high tensile strength and thermal stability. The good comprehensive performance thus provides a solid foundation for hyperbranched polyimides that can be used in soft robotics, drug delivery, and other fields.

Acknowledgements

We gratefully acknowledge the financial support of the National Natural Science Foundation of China (51873233, 51573210), Hubei Provincial Natural Science Foundation of China (2018CFA023), and the Fundamental Research Funds for the Central Universities (CZP18001).

References

- [1] Zhao R., Zhao T., Jiang X., Liu X., Shi D., Liu C., Yang S., Chen E-Q.: Thermoplastic high strain multishape memory polymer: Side-chain polynorbornene with columnar liquid crystalline phase. *Advanced Materials*, **29**, 1605908/1–1605908/6 (2017).
<https://doi.org/10.1002/adma.201605908>
- [2] Zhang X., Tan B. H., Li Z.: Biodegradable polyester shape memory polymers: Recent advances in design, material properties and applications. *Materials Science and Engineering: C*, **92**, 1061–1074 (2018).
<https://doi.org/10.1016/j.msec.2017.11.008>

- [3] Chen H-M., Wang L., Zhou S-B.: Recent progress in shape memory polymers for biomedical applications. *Chinese Journal of Polymer Science*, **36**, 905–917 (2018).
<https://doi.org/10.1007/s10118-018-2118-7>
- [4] Meng H., Li G.: A review of stimuli-responsive shape memory polymer composites. *Polymer*, **54**, 2199–2221 (2013).
<https://doi.org/10.1016/j.polymer.2013.02.023>
- [5] Zhang Z-X., Dou J-X., He J-H., Xiao C-X., Shen L-Y., Yang J-H., Wang Y., Zhou Z-W.: Electrically/infrared actuated shape memory composites based on a bio-based polyester blend and graphene nanoplatelets and their excellent self-driven ability. *Journal of Materials Chemistry C*, **5**, 4145–4158 (2017).
<https://doi.org/10.1039/C7TC00828G>
- [6] Huang W. M., Zhao Y., Wang C. C., Ding Z., Purnawali H., Tang C., Zhang J. L.: Thermo/chemo-responsive shape memory effect in polymers: A sketch of working mechanisms, fundamentals and optimization. *Journal of Polymer Research*, **19**, 9952/1–9952/34 (2012).
<https://doi.org/10.1007/s10965-012-9952-z>
- [7] Jian Y-K., Le X-X., Zhang Y-C., Lu W., Wang L., Zheng J., Zhang J-W., Huang Y-J., Chen T.: Shape memory hydrogels with simultaneously switchable fluorescence behavior. *Macromolecular Rapid Communications*, **39**, 1800130/1–1800130/5 (2018).
<https://doi.org/10.1002/marc.201800130>
- [8] Wang W., Lai H., Cheng Z., Kang H., Wang Y., Zhang H., Wang J., Liu Y.: Water-induced poly(vinyl alcohol)/carbon quantum dot nanocomposites with tunable shape recovery performance and fluorescence. *Journal of Materials Chemistry B*, **6**, 7444–7450 (2018).
<https://doi.org/10.1039/C8TB02064G>
- [9] Feng Z., Zuo H., Gao W., Ning N., Tian M., Zhang L.: A robust, self-healable, and shape memory supramolecular hydrogel by multiple hydrogen bonding interactions. *Macromolecular Rapid Communications*, **39**, 1800138/1–1800138/7 (2018).
<https://doi.org/10.1002/marc.201800138>
- [10] Zhang X., Cox L., Wen Z., Xi W., Ding Y., Bowman C. N.: Implementation of two distinct wavelengths to induce multistage polymerization in shape memory materials and nanoimprint lithography. *Polymer*, **156**, 162–168 (2018).
<https://doi.org/10.1016/j.polymer.2018.09.032>
- [11] Wei Y., Huang R., Dong P., Qi X-D., Fu Q.: Preparation of polylactide/poly(ether)urethane blends with excellent electro-actuated shape memory *via* incorporating carbon black and carbon nanotubes hybrids fillers. *Chinese Journal of Polymer Science*, **36**, 1175–1186 (2018).
<https://doi.org/10.1007/s10118-018-2138-3>
- [12] Wang Y., Ma T., Tian W., Ye J., Wang Y., Jiang X.: Electroactive shape memory properties of graphene/epoxy-cyanate ester nanocomposites. *Pigment and Resin Technology*, **47**, 72–78 (2017).
<https://doi.org/10.1108/PRT-04-2017-0037>
- [13] Liu T., Hao C., Wang L., Li Y., Liu W., Xin J., Zhang J.: Eugenol-derived biobased epoxy: Shape memory, repairing, and recyclability. *Macromolecules*, **50**, 8588–8597 (2017).
<https://doi.org/10.1021/acs.macromol.7b01889>
- [14] Wei M., Zhan M., Yu D., Xie H., He M., Yang K., Wang Y.: Novel poly(tetramethylene ether)glycol and poly(ϵ -caprolactone) based dynamic network via quadruple hydrogen bonding with triple-shape effect and self-healing capacity. *ACS Applied Materials and Interfaces*, **7**, 2585–2596 (2015).
<https://doi.org/10.1021/am507575z>
- [15] Podgórski M., Wang C., Bowman C. N.: Multiple shape memory polymers based on laminates formed from thiol-click chemistry based polymerizations. *Soft Matter*, **11**, 6852–6858 (2015).
<https://doi.org/10.1039/C5SM01260K>
- [16] Xie T.: Tunable polymer multi-shape memory effect. *Nature*, **464**, 267–270 (2010).
<https://doi.org/10.1038/nature08863>
- [17] Walczak J., Sobota M., Chrzanowski M., Krucinska I.: Application of the melt-blown technique in the production of shape-memory nonwoven fabrics from a blend of poly(L-lactide) and atactic poly[(R,S)-3-hydroxy butyrate]. *Textile Research Journal*, **88**, 2141–2152 (2017).
<https://doi.org/10.1177/0040517517716906>
- [18] Zhang Y., Wang C., Pei X., Wang Q., Wang T.: Shape memory polyurethanes containing azo exhibiting photoisomerization function. *Journal of Materials Chemistry*, **20**, 9976–9981 (2010).
<https://doi.org/10.1039/C0JM01944E>
- [19] Guan Q., Picken S. J., Sheiko S. S., Dingemans T. J.: High-temperature shape memory behavior of novel all-aromatic (AB)_n-multiblock copoly(ester imide)s. *Macromolecules*, **50**, 3903–3910 (2017).
<https://doi.org/10.1021/acs.macromol.7b00569>
- [20] Yang Z., Duan C., Sun Y., Wang T., Zhang X., Wang Q.: Utilizing polyhexahydrotriazine (PHT) to cross-link polyimide oligomers for high-temperature shape memory polymer. *Industrial and Engineering Chemistry Research*, **58**, 10599–10608 (2019).
<https://doi.org/10.1021/acs.iecr.9b01405>
- [21] Zhang Y., Li Y., Hu Y., Zhu X., Huang Y., Zhang Z., Rao S., Hu Z., Qiu W., Wang Y., Li G., Yang L., Li J., Wu D., Huang W., Qiu C., Chu J.: Localized Self-growth of reconfigurable architectures induced by a femtosecond laser on a shape-memory polymer. *Advanced Materials*, **30**, 1803072/1–1803072/9 (2018).
<https://doi.org/10.1002/adma.201803072>
- [22] Xu J., Song J.: High performance shape memory polymer networks based on rigid nanoparticle cores. *Proceedings of the National Academy of Sciences*, **107**, 7652–7657 (2010).
<https://doi.org/10.1073/pnas.0912481107>

- [23] Yang Z., Wang Q., Wang T.: Engineering a hyperbranched polyimide membrane for shape memory and CO₂ capture. *Journal of Materials Chemistry A*, **5**, 13823–13833 (2017).
<https://doi.org/10.1039/C7TA02842C>
- [24] Gao H., Li J., Xie F., Liu Y., Leng J.: A novel low colored and transparent shape memory copolyimide and its durability in space thermal cycling environments. *Polymer*, **156**, 121–127 (2018).
<https://doi.org/10.1016/j.polymer.2018.10.001>
- [25] Wang Q., Bai Y., Chen Y., Ju J., Zheng F., Wang T.: High performance shape memory polyimides based on π - π interactions. *Journal of Materials Chemistry A*, **3**, 352–359 (2015).
<https://doi.org/10.1039/C4TA05058D>
- [26] Lan Z., Chen X., Zhang X., Zhu C., Yu Y., Wei J.: Transparent, high glass-transition temperature, shape memory hybrid polyimides based on polyhedral oligomeric silsesquioxane. *Polymers*, **11**, 1058/1–1058/11 (2019).
<https://doi.org/10.3390/polym11061058>
- [27] Bai Y., Mao L., Liu Y.: High temperature shape memory polyimide ionomer. *Journal of Applied Polymer Science*, **133**, 43630/1–43630/8 (2016).
<https://doi.org/10.1002/app.43630>
- [28] Koerner H., Strong R. J., Smith M. L., Wang D. H., Tan L-S., Lee K. M., White T. J., Vaia R. A.: Polymer design for high temperature shape memory: Low crosslink density polyimides. *Polymer*, **54**, 391–402 (2013).
<https://doi.org/10.1016/j.polymer.2012.11.007>
- [29] Yoonessi M., Shi Y., Scheiman D. A., Lebron-Colon M., Tigelaar D. M., Weiss R. A., Meador M. A.: Graphene polyimide nanocomposites; Thermal, mechanical, and high-temperature shape memory effects. *ACS Nano*, **6**, 7644–7655 (2012).
<https://doi.org/10.1021/nn302871y>
- [30] Yao J., Zhang Z., Wang C., Ma S., Li T., Zhao X., Wang D., Zhou H., Chen C.: Multi-shape memory effect of polyimides with extremely high strain. *RSC Advances*, **7**, 53492–53496 (2017).
<https://doi.org/10.1039/C7RA11399D>
- [31] Gao H., Lan X., Liu L., Xiao X., Liu Y., Leng J.: Study on performances of colorless and transparent shape memory polyimide film in space thermal cycling, atomic oxygen and ultraviolet irradiation environments. *Smart Materials and Structures*, **26**, 095001/1–095001/13 (2017).
<https://doi.org/10.1088/1361-665X/aa7bd7>
- [32] Sidra L. R., Chen G., Li C., Mushtaq N., Ma K., Fang X.: Processable, high Tg polyimides from unsymmetrical diamines containing 4-phenoxy aniline and benzimidazole moieties. *Polymer*, **148**, 228–238 (2018).
<https://doi.org/10.1016/j.polymer.2018.06.036>
- [33] Vanherck K., Koeckelberghs G., Vankelecom I. F. J.: Crosslinking polyimides for membrane applications: A review. *Progress in Polymer Science*, **38**, 874–896 (2013).
<https://doi.org/10.1016/j.progpolymsci.2012.11.001>
- [34] Yang Z., Song F., Wang Q., Wang T.: Shape memory induced structural evolution of high performance copolyimides. *Journal of Polymer Science Part A: Polymer Chemistry*, **54**, 3858–3867 (2016).
<https://doi.org/10.1002/pola.28356>
- [35] Kolb H. C., Finn M. G., Sharpless K. B.: Click chemistry: Diverse chemical function from a few good reactions. *Angewandte Chemie International Edition*, **32**, 2005–2021 (2001).
[https://doi.org/10.1002/1521-3773\(20010601\)40:11<2004::AID-ANIE2004>3.0.CO;2-5](https://doi.org/10.1002/1521-3773(20010601)40:11<2004::AID-ANIE2004>3.0.CO;2-5)
- [36] Northrop B. H., Frayne S. H., Choudhary U.: Thiol-maleimide ‘click’ chemistry: Evaluating the influence of solvent, initiator, and thiol on the reaction mechanism, kinetics, and selectivity. *Polymer Chemistry*, **6**, 3415–3430 (2015).
<https://doi.org/10.1039/C5PY00168D>
- [37] Chen S., Xu Z., Zhang D.: Synthesis and application of epoxy-ended hyperbranched polymers. *Chemical Engineering Journal*, **343**, 283–302 (2018).
<https://doi.org/10.1016/j.cej.2018.03.014>
- [38] Zhang D., Liu C., Chen S., Zhang J., Cheng J., Miao M.: Highly efficient preparation of hyperbranched epoxy resins by UV-initiated thiol-ene click reaction. *Progress in Organic Coatings*, **101**, 178–185 (2016).
<https://doi.org/10.1016/j.porgcoat.2016.08.010>
- [39] Liu C., Li T., Zhang J., Chen S., Xu Z., Zhang A., Zhang D.: Preparation and properties of phosphorous-nitrogen containing UV-curable polymeric coatings based on thiol-ene click reaction. *Progress in Organic Coatings*, **90**, 21–27 (2016).
<https://doi.org/10.1016/j.porgcoat.2015.09.004>
- [40] Shibata M., Hashimoto Y.: High performance thermosetting bismaleimide resins via thiol-maleimide ‘click’ reaction. *European Polymer Journal*, **93**, 561–571 (2017).
<https://doi.org/10.1016/j.eurpolymj.2017.06.032>
- [41] Sugane K., Takagi R., Shibata M.: Thermally healable/heat-resistant properties of thermosets bearing dynamic and thermally stable bonds formed by the Diels-Alder and thiol-maleimide ‘click’ reactions. *Reactive and Functional Polymers*, **131**, 211–218 (2018).
<https://doi.org/10.1016/j.reactfunctpolym.2018.08.001>
- [42] Parzuchowski P. G., Gregorowicz J., Wawrzyńska E. P., Wiącek D., Rokicki G.: The phase behavior in supercritical carbon dioxide of hyperbranched copolymers with architectural variations. *The Journal of Supercritical Fluids*, **107**, 657–668 (2016).
<https://doi.org/10.1016/j.supflu.2015.07.028>
- [43] Shi Y-Q., Fu T., Xu Y-J., Li D-F., Wang X-L., Wang Y-Z.: Novel phosphorus-containing halogen-free ionic liquid toward fire safety epoxy resin with well-balanced comprehensive performance. *Chemical Engineering Journal*, **354**, 208–219 (2018).
<https://doi.org/10.1016/j.cej.2018.08.023>

- [44] Rahman M. M., Zainuddin S., Hosur M. V., Robertson C. J., Kumar A., Trovillion J., Jeelani S.: Effect of NH₂-MWCNTs on crosslink density of epoxy matrix and ILSS properties of e-glass/epoxy composites. *Composite Structures*, **95**, 213–221 (2013).
<https://doi.org/10.1016/j.compstruct.2012.07.019>
- [45] Flory P. J.: Principles of polymer chemistry. Cornell University Press, Ithaca (1953).
- [46] Wang L., Liang Y., Yu Q., Chen S., Zhang J., Miao M., Zhang D.: Synthesis of epoxy-ended hyperbranched polyesters with reinforcing and toughening function for diglycidyl ether of bisphenol-A. *Polymer Composites*, **39**, E2046–E2055 (2018).
<https://doi.org/10.1002/pc.24443>
- [47] Li X., Pan Y., Lai J., Wu R., Zheng Z., Ding X.: Design of well-defined shape memory networks with high homogeneity: Towards advanced shape memory polymeric materials. *Polymer Chemistry*, **8**, 3867–3873 (2017).
<https://doi.org/10.1039/C7PY00904F>
- [48] Dailing E. A., Nair D. P., Setterberg W. K., Kyburz K. A., Yang C., D'Ovidio T., Anseth K. S., Stansbury J. W.: Combined, independent small molecule release and shape memory via nanogel-coated thiourethane polymer networks. *Polymer Chemistry*, **7**, 816–825 (2016).
<https://doi.org/10.1039/C5PY01464F>
- [49] Nair D. P., Cramer N. B., Scott T. F., Bowman C. N., Shandas R.: Photopolymerized thiol-ene systems as shape memory polymers. *Polymer*, **51**, 4383–4389 (2010).
<https://doi.org/10.1016/j.polymer.2010.07.027>
- [50] Liu Y., Gall K., Dunn M. L., Greenberg A. R., Diani J.: Thermomechanics of shape memory polymers: Uniaxial experiments and constitutive modeling. *International Journal of Plasticity*, **22**, 279–313 (2006).
<https://doi.org/10.1016/j.ijplas.2005.03.004>
- [51] Ding Z., Yuan L., Liang G., Gu A.: Thermally resistant thermadappt shape memory crosslinked polymers based on silyl ether dynamic covalent linkages for self-folding and self-deployable smart 3D structures. *Journal of Materials Chemistry A*, **7**, 9736–9747 (2019).
<https://doi.org/10.1039/C9TA01147A>
- [52] Chen S., Zhang D., Jiang S., Jia D.: Preparation of hyperbranched epoxy resin containing nitrogen heterocycle and its toughened and reinforced composites. *Journal of Applied Polymer Science*, **123**, 3261–3269 (2011).
<https://doi.org/10.1002/app.35012>